EJNMMI Research

ORIGINAL RESEARCH

Open Access

Intraoperative visualization of nerves using a myelin protein-zero specific fluorescent tracer

Tessa Buckle[1*], Albertus. W. Hensbergen[1], Danny M. van Willigen[1], Frank Bosse[2], Kevin Bauwens[3], Rob C. M. Pelger[4] and Fijs W. B. van Leeuwen[1,3*]

Abstract

Background: Surgically induced nerve damage is a common but debilitating side effect in oncological surgery. With the aim to use fluorescence guidance to enable nerve-sparing interventions in future surgery, a fluorescent tracer was developed that specifically targets myelin protein zero (P0).

Results: Truncated homotypic P0 protein-based peptide sequences were C-terminally functionalized with the far-red cyanine dye Cy5. The lead compound **Cy5-P0$_{101-125}$** was selected after initial solubility, (photo)physical and in vitro evaluation (including P0-blocking experiments). **Cy5-P0$_{101-125}$** ($K_D = 105 \pm 17$ nM) allowed in vitro and ex vivo P0-related staining. Furthermore, **Cy5-P0$_{101-125}$** enabled in vivo fluorescence imaging of the Sciatic nerve in mice after local intravenous (i.v.) administration and showed compatibility with a clinical fluorescence laparoscope during evaluation in a porcine model undergoing robot-assisted surgery. Biodistribution data revealed that i.v. administered **[^{111}In]In-DTPA-P0$_{101-125}$** does not enter the central nervous system (CNS).

Conclusion: **P0$_{101-125}$** has proven to be a potent nerve-specific agent that is able to target P0/myelin under in vitro, ex vivo, and in vivo conditions without posing a threat for CNS-related toxicity.

Keywords: Nerve imaging, Fluorescence-guided surgery, Myelin protein zero, Targeted imaging

Background

Surgery, and science therein, has come a long way since Mr. Gunning and Lord Thurlow, respectively, stated to each other in 1796: "there is no more science in surgery", in reply "than there is in butchery" [1]. Contradictory to these statements, the rapid translation of innovative minimally invasive surgical technologies has initiated the concept of "precision surgery" (2–5). This concept is mostly driven by engineering efforts in the form of medical devices such as endoscopic cameras, refined instruments, and robotic manipulators that enable modern surgeons to intervene in the human body in ways that were previously not thought possible [3, 4, 6]. Imaging provides an alternative to impact surgical accuracy; the application of minimally invasive procedures is strengthened by the ability to map areas of disease in the context of healthy anatomy (so-called surgical roadmaps) using non-invasive preoperative imaging modalities such as MRI or PET/CT [7–9]. Unfortunately, intraoperative detection of preoperatively identified lesions/structures can be challenging. For instance, increased distancing between the surgeon and the patient limits the surgeon's sensory experience in the form of palpation (e.g. when a surgical robot is used). This shortcoming can at least in part be compensated through the use of interventional molecular imaging. To date, this imaging sub-discipline has predominantly focused on intraoperative detection of cancerous lesions using either radio- or fluorescence guidance [10, 11]. Here the main applications have included complex anatomies such as the head-and-neck or pelvic area where image guidance is exploited for both detection of nodal metastases and primary tumour

*Correspondence: t.buckle@lumc.nl; f.w.b.van_leeuwen@lumc.nl
[1] Interventional Molecular Imaging Laboratory, Department of Radiology, Leiden University Medical Center, Albinusdreef 2, 2300 RC Leiden, The Netherlands
Full list of author information is available at the end of the article

margins [12–16]. However, in these same anatomies accidental surgical damage to nerves can yield debilitating side effects such as loss of sensory feeling or speech, incontinence and/or erectile dysfunction. This occurrence of surgically induced nerve damage is not uncommon: despite the fact that more than 70% of prostate cancer patients receive nerve-sparing surgery, it is accepted that 30% of patients suffer from loss of erectile function at 1 year post-surgery [17]. Here, it should be noted that the extent of the damage may be hard to predict [18]. In addition, 10–15% of patients suffer from urinary incontinence [19]. In head and neck cancer patients, nerve anatomies are complex [20] and recurrent laryngeal nerve injury and mandibular nerve injury is seen in 14% of patients undergoing, respectively, thyroid surgery or neck dissection [21, 22]. Permanent paralysis is seen in 4–7% of patients [22].

Nerve-specific fluorescence imaging has been poised as a means to allow high-resolution nerve identification in real time [23]. For this application, a number of different targeting strategies have been evaluated, ranging from neuronal tracing to targeting intracellular expressed proteins in myelin sheets such as myelin basic protein [23–27]. In some cases, the nerve-specific target is unknown [27–30]. When pursuing conventional receptor-targeted molecular imaging strategies, extracellularly expressed targets are generally sought after. In that sense, myelin protein zero (MPZ, or P0), a 124-amino-acid-residues-large homotypic protein that makes up 80% of the protein content in peripheral myelin (Fig. 1A, [31]), and that is located on the outer membrane of the Schwann cells that form the myelin sheath, would most certainly be a target that is worth exploring. Uniquely, P0 is specific for the peripheral nervous system (PNS) and is not expressed in the central nervous system (CNS). In the CNS myelin sheath formation is facilitated by the adhesive properties of myelin proteolipid protein (PLP; [32]).

Building on the truncation of the extracellular portion of P0 (Fig. 1B) that was previously proposed by Makowska et al. [33] and the homotypic binding properties of P0

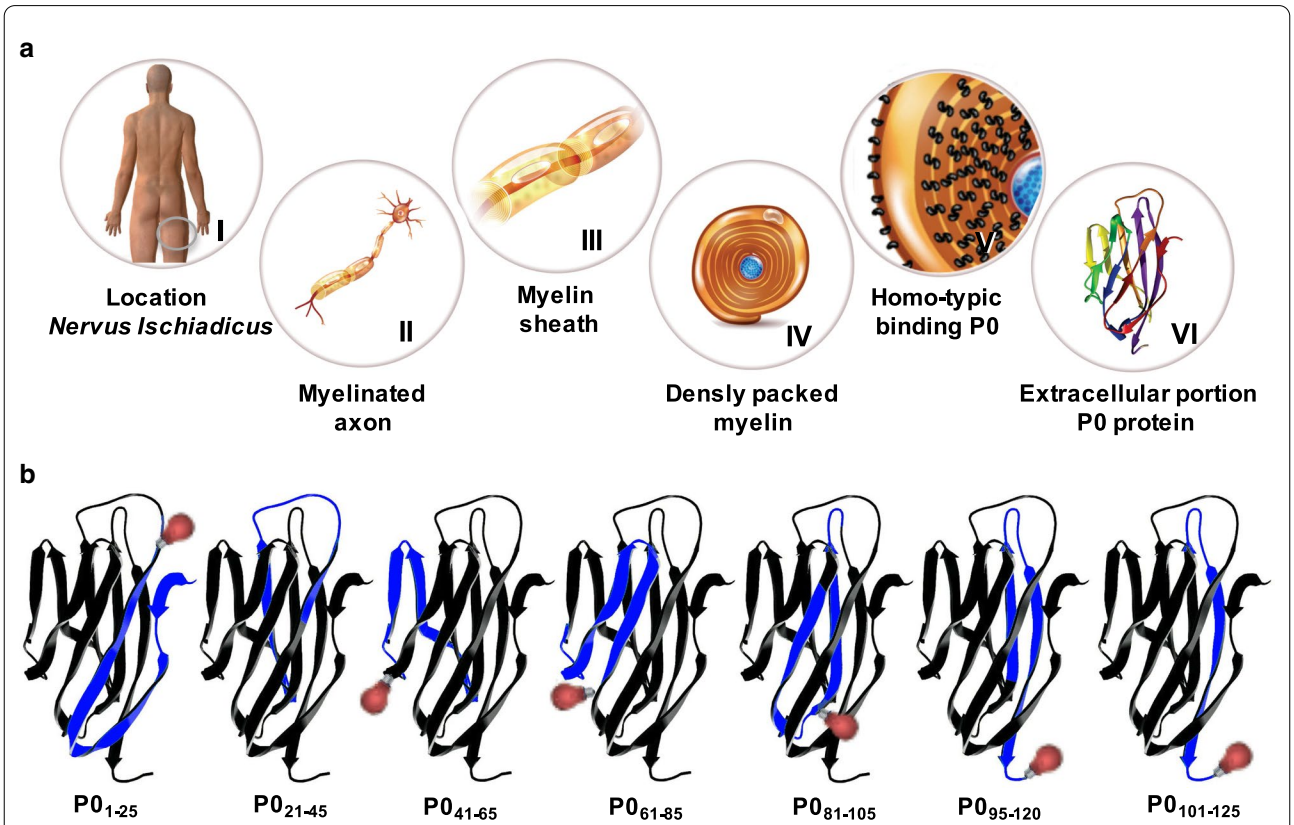

Fig. 1 Myelin protein zero as a target for nerve imaging. **A** schematic overview of the localization of myelin protein zero (P0) in the peripheral nervous system with (I) the location of the *nervus ischiadicus* (encircled in grey), (II) myelinated axon within this nerve, (III) the myelin sheath encapsulating the axon, (IV) densely packed myelin within the myelin sheath, (V) homotypic binding of P0 within the myelin sheath (location P0 on outer membrane and between layers annotated in black) and (VI) the crystal structure of the extracellular portion of P0 ($P0_{ex}$). **B** Peptides $\mathbf{P0_{1-25}}$, $\mathbf{P0_{21-45}}$, $\mathbf{P0_{41-65}}$, $\mathbf{P0_{61-85}}$, $\mathbf{P0_{81-105}}$, $\mathbf{P0_{95-120}}$ and $\mathbf{P0_{101-125}}$ derived from the crystal structure of $P0_{ex}$ with the specific section of the amino acid sequence included in the peptide highlighted in blue and the location of Cy5 functionalization represented by a red-light bulb

(e.g. intrinsic binding between P0 and P0), fluorescently labelled nerve-specific synthetic P0-derived peptides were extrapolated from the crystal structure of P0 (Fig. 1B; peptides in blue). After initial solubility, (photo) physical and in vitro evaluation (affinity and microscopic localization) a lead compound that showed the most ideal properties was selected. This fluorescent tracer was further scrutinized in three-dimensional (3D) dorsal root ganglion (DRG) cell cultures, on ex vivo nerve specimens and in vivo in mice (macroscopic localization, nerve/myelin-specificity, biodistribution). In vivo nerve visualization in a porcine model was performed as a proof of principle for real-time nerve visualization in a robot-assisted surgery setting.

Methods

General chemistry

All chemicals were obtained from commercial sources and used without further purification. DMF was dried over 4 Å molecular sieves. High-pressure liquid chromatography (HPLC) was performed on a Waters HPLC system (Waters Chromatography B.V., Etten-Leur, The Netherlands) using a 1525EF pump and a 2489 UV detector. For preparative HPLC, a Maisch ReproSil-Pur 120 C18-AQ 10 µM (250 mm × 20 mm) column (Dr. Maisch HPLC GmbH, Ammerbuch-Entringen, Germany) was used at a flow rate of 12 mL/min. For analytical HPLC, a Maisch ReproSil-Pur C18-AQ 5 µM (250 mm × 4.6 mm) column was used with a gradient of 0.1% trifluoroacetic acid (TFA) in H_2O/MeCN 95:5 to 0.1% TFA in H_2O/MeCN 5:95 in 20 min (1 mL/min). Low-resolution mass spectrometry (LRMS) was performed on a Bruker Microflex LT/SH MALDI-TOF mass spectrometer using linear mode. High-resolution mass spectrometry (HRMS) was performed on a Waters Acquity H-class UPLC (Waters, Milford, USA) using a Acquity UPLC BEH C18 1.7 µm (2.1 × 50 mm) column with a gradient of 0.1% FA in H_2O/CH_3CN 98:2 to 0.1% FA in H_2O/CH_3CN 60:40 in 1.8 min (0.6 mL/min) coupled to a high-resolution XEVO G2S-XTOF Mass Spectrometer (Waters, Milford, USA). ^{1}H and ^{13}C NMR were performed on a Bruker Ascend 850 (850 MHz) equipped with a CryoProbe (all from Bruker, Billerica, USA) in deuterated solvents. Crude peptides were analysed by a Waters Acquity UPLC-MS system using a Waters BEH C18 1.7 µm, 2.1 × 100 mm column, applying gradient from 5% CH_3CN in H_2O + 0.2% TFA to 75% CH_3CN in 7 min.

Peptide synthesis and Cy5 labelling

The peptides **P0$_{1–25}$**, **P0$_{21–45}$**, **P0$_{41–65}$**, **P0$_{61–85}$**, **P0$_{81–105}$**, **P0$_{95–120}$** and **P0$_{101–125}$** (Fig. 1B, Additional file 1: Table SI1) were synthesized by the peptide production facility of the LUMC employing (robotic) Fmoc SPPS using preloaded Tentagel® S AC resins (Rapp Polymere GmbH, Tübingen, Germany). A pseudoproline method was employed for **P0$_{95–120}$** and **P0$_{101–125}$** [34]. Peptides **P0$_{1–25}$** (52% isolated yield), **P0$_{41–65}$** (41% isolated yield), **P0$_{61–85}$** (22% isolated yield), and **P0$_{81–105}$** (85% isolated yield) could be synthesized in fair yields. **P0$_{95–120}$** and **P0$_{101–125}$** could only be effectively synthesized using pseudoprolines [34], resulting in a 57% and 50% yield. The synthesis of **P0$_{21–45}$** failed repeatedly, meaning this peptide was excluded from further evaluation.

Fluorescent labelling yielding **Cy5-P0$_{1–25}$**, **Cy5-P0$_{41–65}$**, **Cy5-P0$_{61–85}$**, **Cy5-P0$_{81–105}$**, **Cy5-P0$_{95–120}$** and **Cy5-P0$_{101–125}$** (see Additional file1: Scheme SI1) was achieved by dissolving 3.8 µmol of each peptide in phosphate buffer (100 mM, pH 7.4). **Cy5-Maleimide** (3.8 µmol, dissolved in DMF; See Additional file 1: Cy5-Maleimide synthesis) was added, and the reaction mixture was agitated for 2 h at room temperature followed by purification by (semi)preparative HPLC. Fluorescent conjugation yielded **Cy5-P0$_{1–25}$** (3% isolated yield), **Cy5-P0$_{41–65}$** (49% isolated yield), **Cy5-P0$_{61–85}$** (5% isolated yield), **Cy5-P0$_{81–105}$** (35% isolated yield), **Cy5-P0$_{95–120}$** (29% isolated yield), and **Cy5-P0$_{101–125}$** (59% isolated yield). The implementation of the pseudoproline method not only increased the yield when synthesizing **P0$_{101–125}$**, but also increased the labelling yield (resulting in **Cy5-P0$_{101–125}$**): An over sixfold increase in yield (9% isolated yield to 59% isolated yield) was seen after implementing this method; labelling of **P0$_{101–125}$** and purification of **Cy5-P0$_{101–125}$** become more efficient as this peptide could be obtained with less by-products. For more synthetic, analytical and stability details on both the peptides and fluorescent peptides, see Additional file 1: Figure SI1.

Synthesis of labelled control compounds **Cy5-P0$_{ex}$** (based on the extracellular portion of the P0 protein, Fig. 1B), **Cy5-P0$_{Ab\text{-}H60}$** (fluorescent variant of the anti P0 antibody clone H60 (**P0$_{Ab\text{-}H60}$**)) and **Cy5-NP41** (based on the non-P0 staining peptide NP41 [27], and **DTPA-P0$_{101–125}$** (including its radiolabelling yielding [**^{111}In**]**In-DTPA-P0$_{101–125}$**) is described in Additional file 1: synthesis of control compounds.

Detailed analysis of the selected lead compound Cy5-P0$_{101–125}$

Cy5-P0$_{101–125}$ was selected as lead compound and subjected to more detailed chemical analysis. Methods and results for assessment of the (photo)physical properties of **Cy5-P0$_{101–125}$** (i.e. serum protein binding and $LogP_{o/w}$, chemical stability, stability at different temperatures and the molar extinction coefficient and relative quantum

yield and brightness) are described in Additional file 1: chemical properties.

Cells and animal models

P0-expressing RT4 D6P2T myelinating Schwannoma cells (ATCC® CRL-2768™; [35]) and non-P0-expressing MDAMB 468 human breast cancer cells (ATCC® HTB-132™) were grown in Dulbecco's modified Eagle medium (Life Technologies, UK) containing penicillin, streptomycin and foetal calf serum (All BD Biosciences) at 37 °C and 5% CO_2.

In line with their use by Whitney et al. [27], transgenic B6.Cg-Tg(Thy1-YFP)-16Jrs/J (THY-1 YFP) mice were obtained from JAX (the Jackson Laboratory) and were used for ex vivo and in vivo nerve staining and in vivo biodistribution studies (8–15 weeks old). THY-1 YFP mice express spectral variants of GFP (yellow fluorescent protein—YFP; ex 488, em 520) at high levels in motor and sensory neurons. The fluorescent signal in the nerves was used as an internal control for the staining (pattern) of the developed imaging agents. Balb/c nude mice were used as non-fluorescent control.

Flow cytometry

Analysis of the binding affinity (K_D) of **Cy5-P0$_{1-25}$**, **Cy5-P0$_{41-65}$**, **Cy5-P0$_{61-85}$**, **Cy5-P0$_{81-105}$**, **Cy5-P0$_{95-120}$** and **Cy5-P0$_{101-125}$** for P0 was performed using P0-expressing RT4 D6P2T cells and a previously described flow cytometric method [36]. For saturation, binding experiments were performed for each of the fluorescent peptides in a concentration range of 0–2000 nM. All measurements were taken in triplicate, and experiments were repeated at least three times per tracer. Fluorescence was measured using a FACSCanto II flow cytometry device (BD Biosciences) in the APC-A channel. The normalized geometric means were fitted with equations in the GraphPad Prism 5 software. A fluorescence-linked immunoabsorbent assay (FLISA) that was used to confirm the specificity of **Cy5-P0$_{101-125}$** for P0 is described in Additional file 1: Fluorescence-linked immunoabsorbent assay.

Fluorescence microscopy of cells

Cells were trypsinized and seeded onto 35-mm culture dishes that contained a glass insert (MatTek co) on the day prior to the imaging experiment.

To all samples, 1 mL medium containing 1 µM **Cy5-P0$_{1-25}$**, **Cy5-P0$_{21-45}$**, **Cy5-P0$_{41-65}$**, **Cy5-P0$_{61-85}$**, **Cy5-P0$_{81-105}$**, **Cy5-P0$_{95-120}$**, or **Cy5-P0$_{101-125}$** was added at one hour prior to imaging (incubation at 4 °C; $N=3$ per tracer). Peptide solutions were sonicated for 20 s prior to addition, in order to prevent aggregation of the peptides in solution. Cy5-functionalized derivatives of a P0-specific antibody (**Cy5-P0$_{Ab-H60}$**), the extracellular portion of P0 (**Cy5-P0$_{ex}$**) as well as a non-P0-specific peptide (**Cy5-NP-41**) and non-functionalized **Cy5-Maleimide** were used as controls (1 µM). A lysosomal (lysotracker green; 2 µL/mL, DND-26, Thermo Fisher) and nuclear stain (Hoechst 33342; 1 mg/mL, Thermo Fisher) were added as means to localize the cell nucleus and intracellular lysosomes. For blocking studies, 5 µL of a 1 mg/mL solution of non-functionalized $P0_{Ab}$ was added to the cells one hour prior to addition of **Cy5-P0$_{101-125}$**. The synthesis of the control compounds is described in the methods section of Additional file 1: Synthesis of control compounds.

In vitro and ex vivo fluorescence confocal images were acquired using a Leica SP8 WL at sequential settings and 10 × or 63 × magnification. Image analysis was performed using Leica Confocal Software (Leica Microsystems). For blocking studies, quantification of the fluorescence signal intensity ($N=10$ for blocked and non-blocked) in the obtained images was performed using ImageJ according to previously described methods [37, 38]. Statistical evaluation was performed based on a Student's t test.

More detailed ex vivo and in vivo studies with lead compound Cy5-P0$_{101-125}$

Culture and imaging of 3D dorsal root ganglion (DRG) explant cultures from THY-1 YFP mouse embryos

For evaluation of the staining pattern of P0, 3D DRG explant cultures were used (all $N=3$ per peptide or control staining). Description of the methods used for ex vivo culture and imaging of 3D DRG explant cultures from THY-1 YFP mouse embryos are provided in Additional file 1: 3D culture of DRG explants. **Cy5-P0$_{Ab-H60}$**, **Cy5-P0$_{ex}$** as well as **Cy5-NP-41** were used as controls.

Ex vivo tissue of mice

Fluorescence immunohistochemistry was performed on fresh frozen samples of the *nervus ischiadicus* that were embedded in Tissue-Tek and cut into 5 µM frozen sections. Cryo-sections were fixed in pre-cooled acetone (VWR Chemicals, 67-64-1) for 10 min and dried on air for 1 h and washed with 1 × phosphate-buffered saline (PBS) (Life Technologies, 10010-015) to remove Tissue-Tek. Slides were incubated for one hour at room temperature with 1 µM of **Cy5-P0$_{101-125}$**. Sections were rinsed and dehydrated using ethanol and mounted with ProLong Gold Antifade Mountant with DAPI (Fisher, P-36931). Images were obtained using a fluorescence confocal microscope. Standard antibody-based immunohistochemistry was used as control; for details, see Additional file 1: Immunohistochemistry.

For direct ex vivo assessment of freshly excised, non-treated tissue non-fixed sections of the *nervus ischiadicus* (mouse; $N=3$) were incubated in 1.5-mL vials (Eppendorf, Falcon) containing 1 µM **Cy5-P0$_{101-125}$** for

1 h. Confocal imaging was performed after washing with PBS. Non-incubated sections of the nerve were used as control.

In vivo assessment in mice

For evaluation of in vivo staining in mice, **Cy5-P0$_{101-125}$** was administered (20 µL; 5 nmol) either intravenously in the v. femoralis or directly into the nerve sheath (intraneural) of THY-1 TFP mice ($N=3$ per injection method) or Balb/c nude mice. Injection was performed under general anaesthetics (hypnorm/dormicum/H_2O solution (1:1:2; 5 µL/g) via intraperitoneal injection). After placement of the mouse in the microscope stand, images were collected prior and during the dissection of the *Nervus Ischiadicus*. Staining was evaluated at 1 h after injection; $N=3$. Mice were killed via cervical dislocation before the start of the imaging session. Animals that received no tracer or that received an intravenous (v. femoralis) injection of **Cy5-NP-41** were used as control. In vivo fluorescence confocal microscopy was performed using a Zeiss 710 NLO upright confocal microscope. For collection and evaluation of the in vivo images, ZEN 2011 software was used. Furthermore, the *nervus ischiadicus* (in vivo; mouse model) and the Pudendal Nerve (excised after in vivo imaging; porcine model) were imaged using a Dino-lite handheld digital fluorescence microscope (AM4115T-DFRW for Cy5 imaging; Dino-lite Digital Microscope; λ_{ex} 620 nm, λ_{em} 650 nm). In-house developed image-processing software [39] that allowed colour coding of the fluorescence signal for improved visualization and distinction of intensity differences was used to depict the nerve-to-background ratio (NBR; ratio between relative fluorescence units in the tumour and surrounding tissue). The provided pseudo-coloured fluorescence overlay was accompanied by an intensity-based scalebar representing the NBR (fluorescence signal intensity differences represented via a colour spectrum). Confirmation of the TBR values was obtained using ImageJ software by dividing the fluorescent signal intensity in the tumour by the fluorescent signal intensity in background tissue.

Biodistribution of [^{111}In]In-DTPA-P0$_{101-125}$ in mice

Synthesis and radiolabelling of **DTPA-P0$_{101-125}$** with ^{111}In is described in Additional file 1: synthesis of control compounds. For quantitative assessment of the biodistribution of **[^{111}In]In-DTPA-P0$_{101-125}$**, 10 MBq of the labelled tracer was injected intravenously (tail vein). The percentage of the injected activity per gram of tissue (%IA/g) was assessed at 2 h post-injection as previously described [40, 41]. Excretion was defined as: (MBq present in animal at 24 h post-tracer administration/injected activity) * 100%.

In vivo assessment in a porcine model

To evaluate whether **Cy5-P0$_{101-125}$** (100 µg, 25.6 nmol) was compatible with a real-life surgical setting, its use evaluated was in a porcine model undergoing robot-assisted surgery using a da Vinci Si or Xi system (Intuitive). Pigs ($N=3$) were injected directly in the Pudendal nerve (intraneural administration). Using a prototype and Cy5 dedicated KARL STORZ fluorescence laparoscope [42] introduced through the assistant trocar, a similar set-up was initially applied in the clinical setting [43, 44]; fluorescence imaging of the nerve and surrounding tissues was performed at 1 h after tracer administration. Animals were maintained under Isoflurane anaesthesia for the complete duration of the surgical training and subsequent nerve imaging experiments and were euthanized before awakening from the anaesthesia. After resection, fluorescence microscopy images were made of the fresh nerve to confirm staining. Image processing was performed using in-house custom-developed software as described above.

Table 1 Fluorescently labelled P0 peptides, sequences and outcome synthesis

Peptide	Amino acid sequence	Negative/positive charges	Solubility in H_2O (µM)	K_D in nM
Cy5-P0$_{1-25}$	H-IVVYTDREVHGAVGSQVTLHC(Cy5)SFWS-NH_2	4+/4−	12	> 1000
Cy5-P0$_{41-65}$	Ac-PEGGRDAISIFHYAKGQPYIDEVGTC(Cy5)-NH_2	3+/7−	45	> 1000
Cy5-P0$_{61-85}$	Ac-DEVGTFKERIQWVGDPRWKDGSIVIC(Cy5)-NH_2	5+/8−	6	> 1000
Cy5-P0$_{81-105}$	Ac-GSIVIHNLDYSDNGTFTC(Cy5)DVKNPPD-NH_2	2+/6−	68	> 1000
Cy5-P0$_{95-120}$	Ac-TFT*A*DVKNPPDIVG**KT**SQ**VT**LYVFEKC(Cy5)-NH_2[a]	4+/5−	150	> 1000
Cy5-P0$_{101-125}$	Ac-KNPPDIVG**KT**SQ**VT**LYVFEKVPTRYC(Cy5)-NH_2[a]	4+/6−	172	105 ± 17

[a] Italic alanine residue replacing the cysteine from native P0, bolded and underlined residues were implemented via the above-mentioned pseudoproline method [34], underlined cysteines were non-native residues added to the C-terminus

Results

Peptide synthesis

As can be seen in Table 1 and Additional file 1: Scheme SI1, the various P0-peptides contain multiple amino acids that can drive self-association through ionic interactions, hydrogen bonding, hydrophobic- and van der Waals interactions [45]. These interactions may play a role in peptides **Cy5-P0$_{41-65}$**, **Cy5-P0$_{61-85}$**, and **Cy5-P0$_{81-105}$** forming particles in solution. Although sonication could be used to (partially) overcome this aggregation, **Cy5-P0$_{95-120}$** and **Cy5-P0$_{101-125}$** show a 2- to 29-fold higher solubility which promotes their use.

In vitro analysis

Quantitative assessment of the binding affinity based on saturation binding experiments revealed a nanomolar (or submicromolar) binding constant (K_D) of 105 ± 17 nM for **Cy5-P0$_{101-125}$** (Additional file 1: Figure SI3A/B, Table 1). For the five other Cy5-P0 peptides within the matrix K_D values of > 1000 nM was found (Table 1).

Fluorescence confocal microscopy of P0-expressing Schwannoma cells revealed clear differences in staining patterns between the tracers (Fig. 2A). While no clear staining was seen for **Cy5-P0$_{1-25}$**, **Cy5-P0$_{41-65}$**, **Cy5-P0$_{61-85}$** or **Cy5-P0$_{85-105}$** (Fig. 2A I–IV), staining of the Schwannoma cells with **Cy5-P0$_{95-120}$**, and especially **Cy5-P0$_{101-125}$** resulted in a densely spotted pattern on both the cell body and the cell outgrowths (Fig. 2A V and VI; Cy5 in red). **Cy5-P0$_{101-125}$** was superior in both the degree of staining and signal intensity, which helped finalize its selection as lead compound. 3D assessment of the cell specimens confirmed that localization of staining of **Cy5-P0$_{101-125}$** was distinctly different to that of lysosomes, confirming extracellular, instead of intracellular, staining (Fig. 2B I and Additional file 1: Figure SI4). The location of **Cy5-P0$_{101-125}$** accumulation was in agreement with staining of an anti-P0 antibody (**Cy5-anti-P0$_{Ab-H60}$**; Fig. 2B II) as well as staining with the extracellular portion of P0 (**Cy5-P0$_{ex}$**; Fig. 2B III). P0-related staining was not seen with the non-P0-specific control peptide (**Cy5-NP41**; Fig. 2B IV; [27]) nor was a similar staining seen in P0-negative cells stained with **Cy5-P0$_{101-125}$** (Fig. 2B V), **Cy5-anti-P0$_{Ab-H60}$** (Fig. 2B VI) or when the non-functionalized Cy5-Maleimide dye was applied (Fig. 2C I).

Blocking experiments revealed the specificity of **Cy5-P0$_{101-125}$** for P0 (Fig. 2CII and III); Quantification of the fluorescence intensity of **Cy5-P0$_{101-125}$** with (Fig. 2CIII, in red) or without addition of $P0_{Ab}$ (in black) showed that only 13.5 ± 7.1% of Cy5-related fluorescence that can be contributed to binding of **Cy5-P0$_{101-125}$** remained after blocking ($p = 0.001$). A customized FLISA set-up further underlined the specificity of **Cy5-P0$_{101-125}$** for P0 by confirming the binding to the extracellular portion of P0 ($P0_{ex}$) for both **Cy5-P0$_{101-125}$** and **Cy5-P0$_{Ab-H60}$**. No binding was observed for the non-P0-specific control **Cy5-NP41** (Additional file 1: Figure SI3).

More detailed studies with lead compound Cy5-P0$_{101-125}$

Chemical analysis

Chemical analysis of **Cy5-P0$_{101-125}$** revealed that this tracer was 99% stable after incubation in serum for 24 h at 37 °C and > 99% stable at temperatures > 0 °C for at least 4 h (Additional file 1: Figure SI2). Additional chemical- and photophysical features of **Cy5-P0$_{101-125}$** are presented in Additional file 1: Table SI2.

Imaging of 3D dorsal root ganglion (DRG) explant cultures from THY-1 YFP mouse embryos

3D cultures based on DRG explants obtained from THY-1 YFP mouse embryos provided an intermediate step between in vitro and in vivo evaluation (Fig. 3A, B). These 3D cultures contained a centre ganglion (*) and axonal outgrowths (white arrow) and are known as well-established neuronal cultures for drug discovery for neuronal neuropathies [46]. Incubation with **Cy5-P0$_{101-125}$** resulted in a spotted staining pattern of cells residing along the course of the developed axonal outgrowths as well as in the DRG explant itself (Fig. 3AII and AIII). Again, staining with **Cy5-P0$_{ex}$** (Fig. 3AIII and BIII) confirmed the findings.

Ex vivo assessment of murine nerve tissue

Immunohistochemical assessment of concurrent fresh-frozen sections of the *nervus ischiadicus* of THY1-YFP mice revealed a clear overlap between the location of P0 between staining obtained after incubation with **Cy5-P0$_{101-125}$** (fluorescence immunohistochemistry; Fig. 3C) and an anti-P0 antibody (standard immunohistochemistry; insert Fig. 3C).

More detailed microscopic assessment of viable (non-frozen, non-pretreated) samples of the *nervus ischiadicus* that were incubated ex vivo with **Cy5-P0$_{101-125}$** revealed an identical wavy staining pattern (Fig. 4AI; in red). Here, the intrinsic YFP signal within the axons of the THY-1 YFP mice provided an extra confirmation that staining of **Cy5-P0$_{101-125}$** co-localized with the myelin sheath surrounding the axons.

In vivo assessment in mice

To reduce the dose and staining beyond the area of interest, in vivo administration intraneural (Fig. 4AII) and

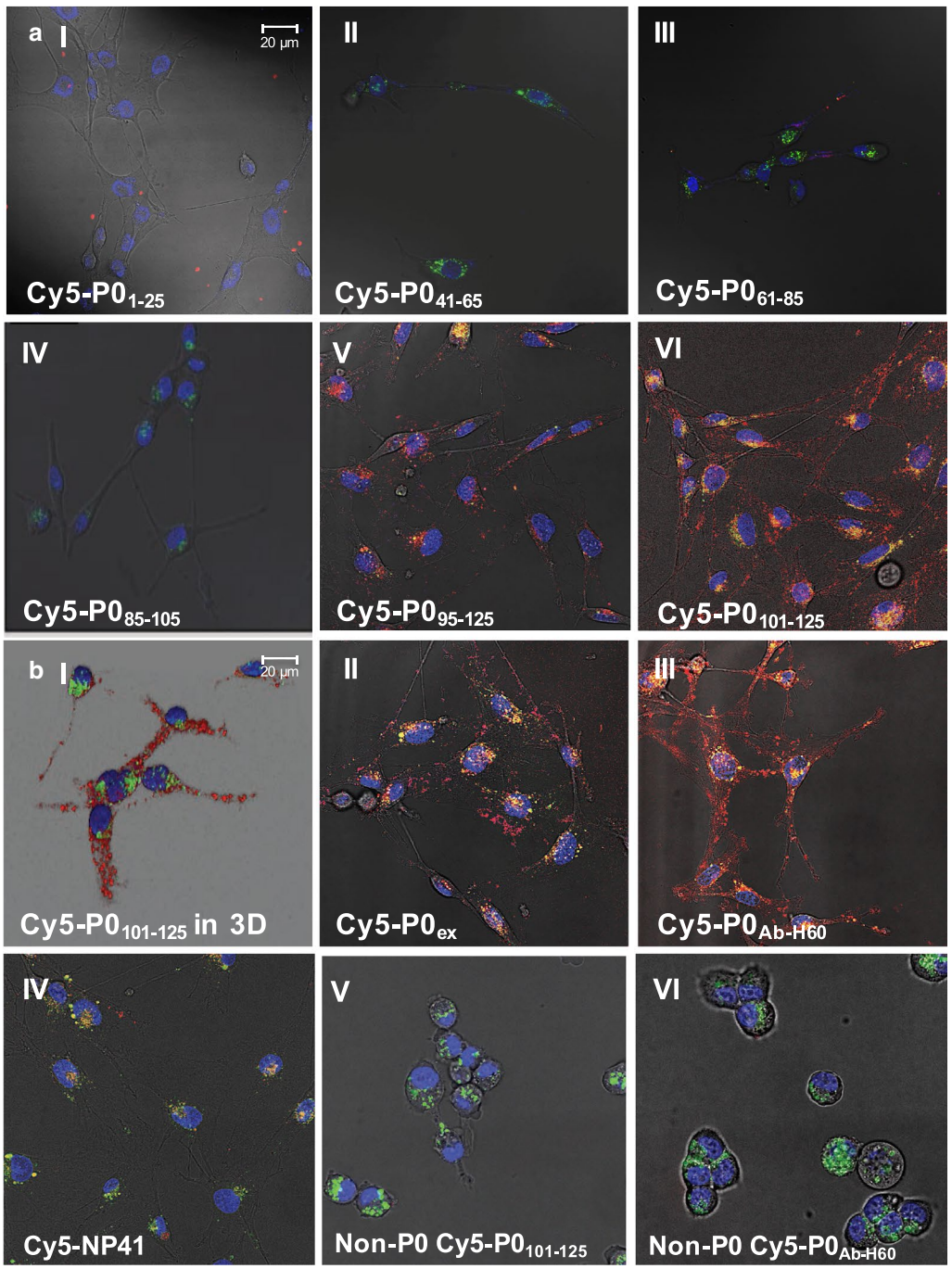

Fig. 2 Localization of binding of P0 peptides to myelinating Schwannoma cells. Fluorescence confocal images of RT4 D6P2T Schwannoma cells after incubation with **A** C-terminally Cy5-labelled $P0_{1-25}$(**Cy5-P0$_{1-25}$**; I), $P0_{41-65}$ (**Cy5-P0$_{41-65}$**; II), $P0_{61-85}$ (**Cy5-P0$_{61-85}$**; III), $P0_{85-105}$(**Cy5-P0$_{185-105}$**; IV), $P0_{95-120}$ (**Cy5-P0$_{95-125}$**; V) or $P0_{101-125}$ (**Cy5-P0$_{101-125}$**; VI). **B** Fluorescence confocal images of RT4 D6P2T Schwannoma cells after incubation with **Cy5-P0$_{95-120}$** represented in 3D (I), and the extracellular portion of P0 (**Cy5-P0$_{ex}$**; II), Cy5-labelled anti-P0 antibody clone H60 (**Cy5-P0$_{Ab-H60}$**; III), a non-P0-specific peptide (**Cy5-NP41**; IV). Staining of non-P0-expressing MDAMB 468 cells with **Cy5-P0$_{101-125}$** (V), **Cy5-P0$_{Ab}$** (VI) and Cy5-Maleimide (CI) were used to show specificity for P0. Blocking experiments showed a clear decrease in the mean fluorescence intensity for **Cy5-P0$_{101-125}$** after pre-incubation with $P0_{Ab}$ (II). Quantification of fluorescence intensity with and without blocking (III; **Cy5-P0$_{101-125}$** in red, blocked conditions in black) further underlined specificity ($p = 0.001$). In all confocal images, Cy5 is represented in red, nuclear staining (Hoechst) in blue and lysosomes (lysotracker green) in green

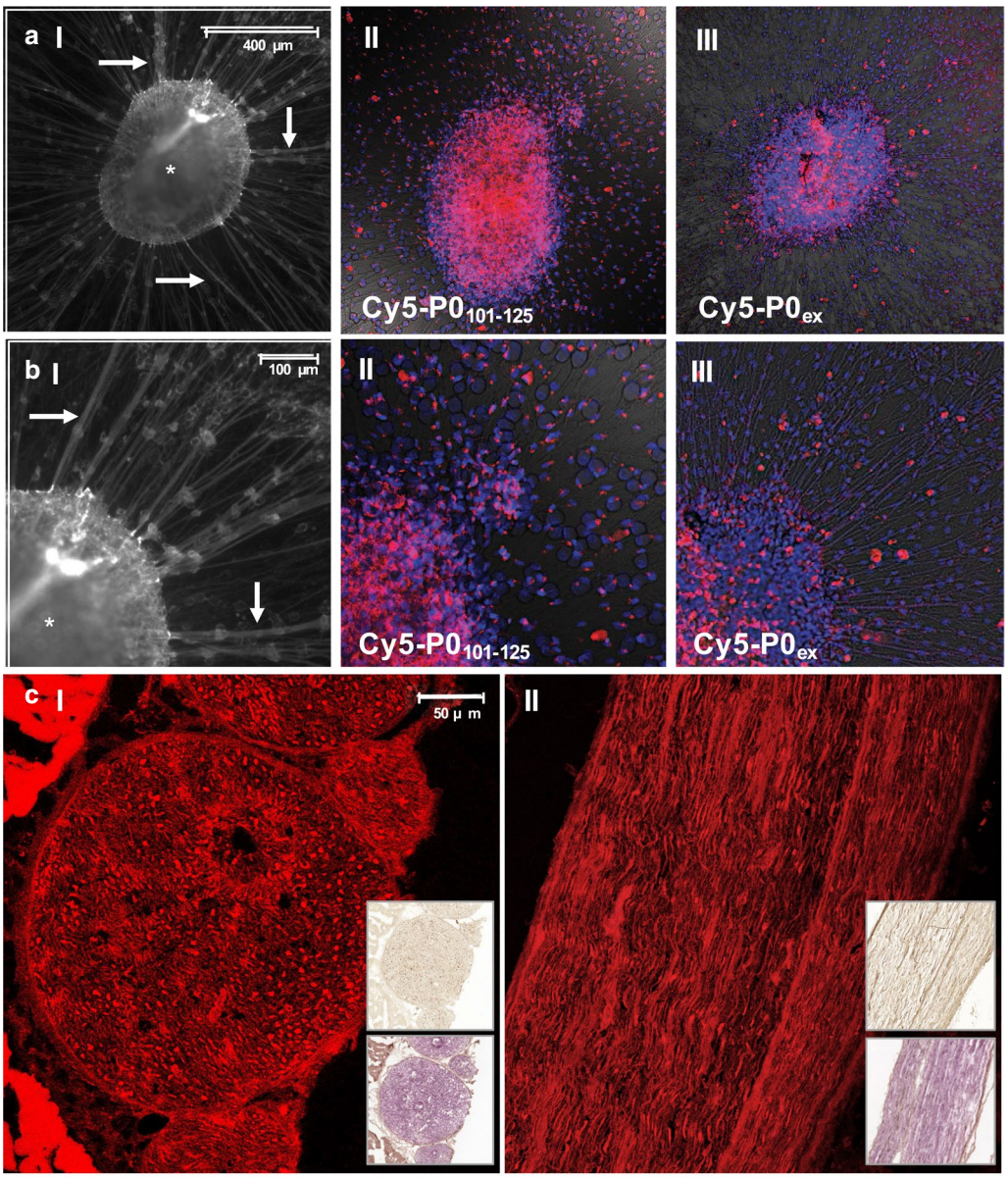

Fig. 3 Staining of 3D DRG explant cultures with Cy5-P0$_{101–125}$ and Cy5-P0$_{101–125}$ fluorescence immunohistochemistry of a murine *nervus ischiadicus*. **A** brightfield image of a 3D DRG explant (*) with axonal outgrowths (white arrow) after staining with (II) **Cy5-P0$_{101–125}$** or (III) **Cy5-P0$_{ex}$**. **B** Zoom-in with focus on the axonal outgrowths and fluorescence confocal imaging of DRG explants after staining with (II) **Cy5-P0$_{101–125}$** or (III) **Cy5-P0$_{ex}$**. **C** Fluorescence immunohistochemistry of the *nervus ischiadicus* of THY1-YFP mice in (I) transverse orientation and (II) sagittal orientation after staining with **Cy5-P0$_{101–125}$**. The top insert shows standard anti-body-based standard immunohistochemistry and the bottom insert H&E staining of a concurrent/adjacent tissue section

intravenous (v. femoralis; Fig. 4AIII and B) administration were applied. Both tracer administration routes provided identical results compared to ex vivo incubation with **Cy5-P0$_{101–125}$**. Similar to assessment in vitro (Fig. 2), the non-P0-specific peptide **CY5-NP41** (Fig. 4AIV) did not provide staining corresponding to the location of myelin after intravenous administration (v. femoralis). Intraoperative fluorescence confocal microscopy after administration of **Cy5-P0$_{101–125}$** allowed clear visualization of the

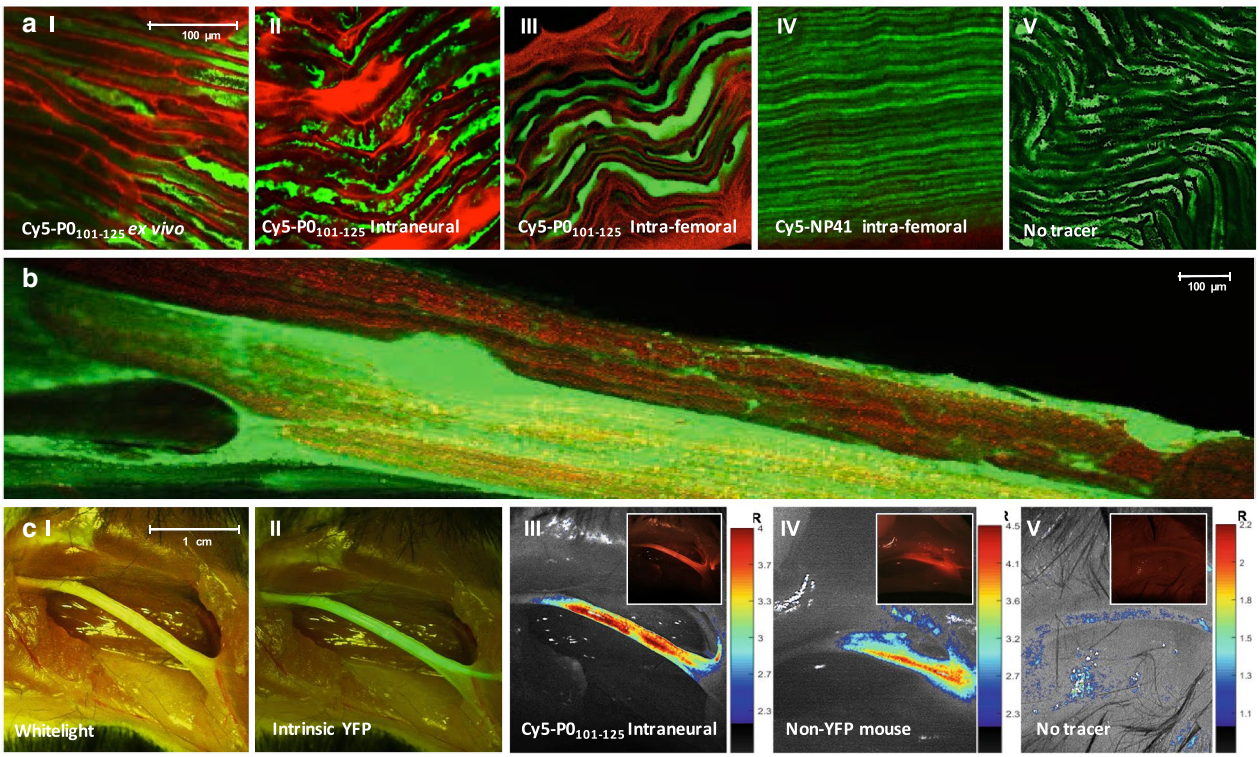

Fig. 4 Ex vivo and in vivo imaging of the *nervus ischiadicus* of mice. **A** 63 × magnification of the *nervus ischiadicus* after (I) ex vivo incubation, (II) intraneural administration or (III) intravenous (v. femoralis) administration of **Cy5-P0$_{101–125}$**. (IV) Fluorescence confocal image of the *nervus ischiadicus* **F** after intravenous (v. femoralis) administration of **Cy5-NP41** or (V) when no tracer was applied. **B** In vivo fluorescence confocal image of a large field of view of the *nervus ischiadicus* of a THY-1 YFP at 1 h after intravenous (v. femoralis) administration of **Cy5-P0$_{101–125}$**. Cy5 in red and intrinsic YFP located in the axons of THY-1 YFP mice in green. **C** In vivo Dinolight microscopy images showing (I) a whitelight image of the *nervus ischiadicus* and (II) the intrinsic YFP signal in a THY-1 YFP mouse. Image processing after illumination of the *nervus ischiadicus* after intraneural administration of **Cy5-P0$_{101–125}$** in (III) a THY-1 YFP mouse, (IV) a non-YFP Balb/c nude mouse and (V) when no tracer was applied. Inserts show unprocessed fluorescence image. Scalebar represents the nerve-to-background ratio (NBR)

nervus ischiadicus based on the emitted fluorescence signal (Fig. 4B).

Macroscopic in vivo assessment of the *nervous ischiadicus* (whitelight image; Fig. 5C) resulted in a mean NBR of 6.0 ± 2.2 after administration of **Cy5-P0$_{101–125}$** (Fig. 4CIII). Comparable results in non-YFP mice (Fig. 5CIV; mean NBR: 3.7 ± 1.0) help exclude the possibility of spectral overlap between YFP and Cy5.

Biodistribution (mouse)

Radiolabelling of **DTPA-P0$_{101–125}$** with ^{111}In (yielding **[^{111}In]In-DTPA-P0$_{101–125}$**) allowed quantitative assessment of the biodistribution at 1 and 4 h after intravenous tracer administration (Fig. 5). At both time points (1 and 4 h) renal clearance, low overall tissue uptake (in %IA/g) and a substantial level of excretion were seen. Most importantly, uptake in the CNS was neglectable (0.12 ± 0.03%IA/g at 4 h p.i.).

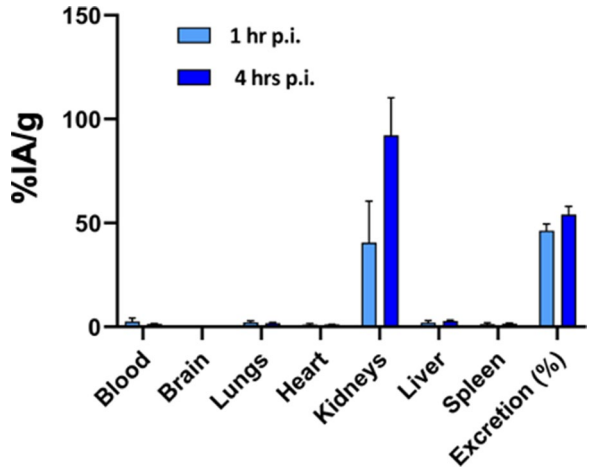

Fig. 5 In vivo biodistribution. Quantitative in vivo biodistribution and excretion of **[^{111}In]In-DTPA-P0$_{101-125}$** at 1 (light blue) and 4 h (dark blue) post-intravenous tracer administration (tail vein). Uptake per organ presented as percentage of the injected activity per gram of tissue (%IA/g). Excretion was defined as: (MBq present in animal at 24 h post-tracer administration/injected activity) * 100%

In vivo assessment in a porcine model

The compatibility of **Cy5-P0$_{101-125}$** with clinical grade imaging modalities applied during robot-assisted minimally invasive surgery was evaluated in a porcine model (Fig. 6). Here, the use of a dedicated Cy5 fluorescence laparoscope (KARL STORZ; [42]) allowed in vivo visualization of the pudendal nerve (Fig. 6B, C; white arrow). Image processing based on colour coding of the fluorescence signal helped assess differences in fluorescence intensity along the nerve (Fig. 6C insert). Back-table imaging of the excised specimen confirmed the fluorescence of the nerve (Fig. 6D).

Discussion

By using the P0-derived synthetic peptide **Cy5-P0$_{101-125}$**, we were able to explore the homotypic P0 protein as molecular target that is widely expressed in myelin in the PNS. Specific binding was demonstrated in vitro, in 3D DRG nerve cultures, ex vivo, as well as in vivo.

Truncation of the homotypical P0-protein into peptides yielded **Cy5-P0$_{101-125}$** as lead compound. In vitro and in vivo studies indicate that this compound is able to provide nerve-specific staining with nanomolar affinity, which is in the same range as reported affinities for other fluorescently labelled targeted tracers [36, 47, 48]. Specificity of **Cy5-P0$_{101-125}$** for P0 was shown both in vitro (Fig. 2 and Additional file 1: Figure SI3) and in vivo (Fig. 4). An approximate 90% decrease in fluorescence intensity after pre-incubation with a P0-specific antibody was seen (Fig. 2CIII), while no staining was observed for the non-P0-specific control (**Cy5-NP41**) and the free dye (Cy5-Maleimide). As the Cy5-Maleimide dye variant was used for functionalization of both P0$_{101-125}$ and NP41, these results also exclude a targeting effect of the dye itself. This was corroborated by a markedly different staining pattern using free dye alone [30]. An additional beneficial factor for **Cy5-P0$_{101-125}$** is that the production is scalable and can be done at reasonably low cost. Moreover, the peptide benefits from the superior pharmacokinetics that have been claimed for peptides over proteins such as antibodies [49, 50].

In line with P0 expression, biodistribution studies performed with the radiolabelled analogue **[^{111}In]In-DTPA-P0$_{101-125}$** helped rule out accumulation of **P0$_{101-125}$** (MW = 3024 Da) in the CNS. Obviously, the chance of toxic side effects is also impacted by dosing and uptake in non-target organs. In nuclear medicine, disease-specific tracers are therefore applied using a micro-dosing regimen (< 100 µg/patient). Although the ability of using fluorescence at micro-dosing levels looks promising [51], this topic remains a subject of debate [52], and many studies still use high dosing regimens to realize in vivo functionalization of molecular targets [16, 53–55]. Local tracer deposition (an image-guided surgery concept that has proven valuable in e.g. lymphatic mapping and during occult lesion localization) limits dosing to 100 µg/patient [12, 51]. Recent experimental studies underscore that local deposition may also be valid when targeting peripheral nerves within a certain surgical anatomy [24, 37]. Substantiated by previous reports [28] Fig. 4 AIII and B indicate that local tracer administration is feasible for nerve imaging applications.

While most image-guided surgery studies promote the use of near-infrared (NIR) Cy7 analogues [53, 54, 56], far-red Cy5-labels are also increasingly being applied in clinical trials [39, 57–59]. In fact, fluorescence-guided surgery trials have been reported for the full fluorescent light spectrum [60]. Uniquely, in a head-to-head comparison, Cy5 analogues even were shown to outperform Cy7-analogies in terms of signal intensity [42] and impact on tracer kinetics [36]. Moreover, Cy5 analogues, both a free dye and conjugated to a peptide, have shown to have a high fluorescence brightness in the presence of human serum albumin (Additional file 1: Table SI2; [36, 41, 61]). These factors combined with the fact that most groups are creating tumour-receptor-targeted tracers using NIR Cy7 analogues support the future implementation of multi-wavelength imaging applications, a concept that is gaining traction in the clinic [60].

Although intraneural injection provides a perfect proof of principle in both mice and pigs (Figs. 4AII, C and Additional file 1: Figure SI6), administration into a blood vessel near the target organ, such as the femoral

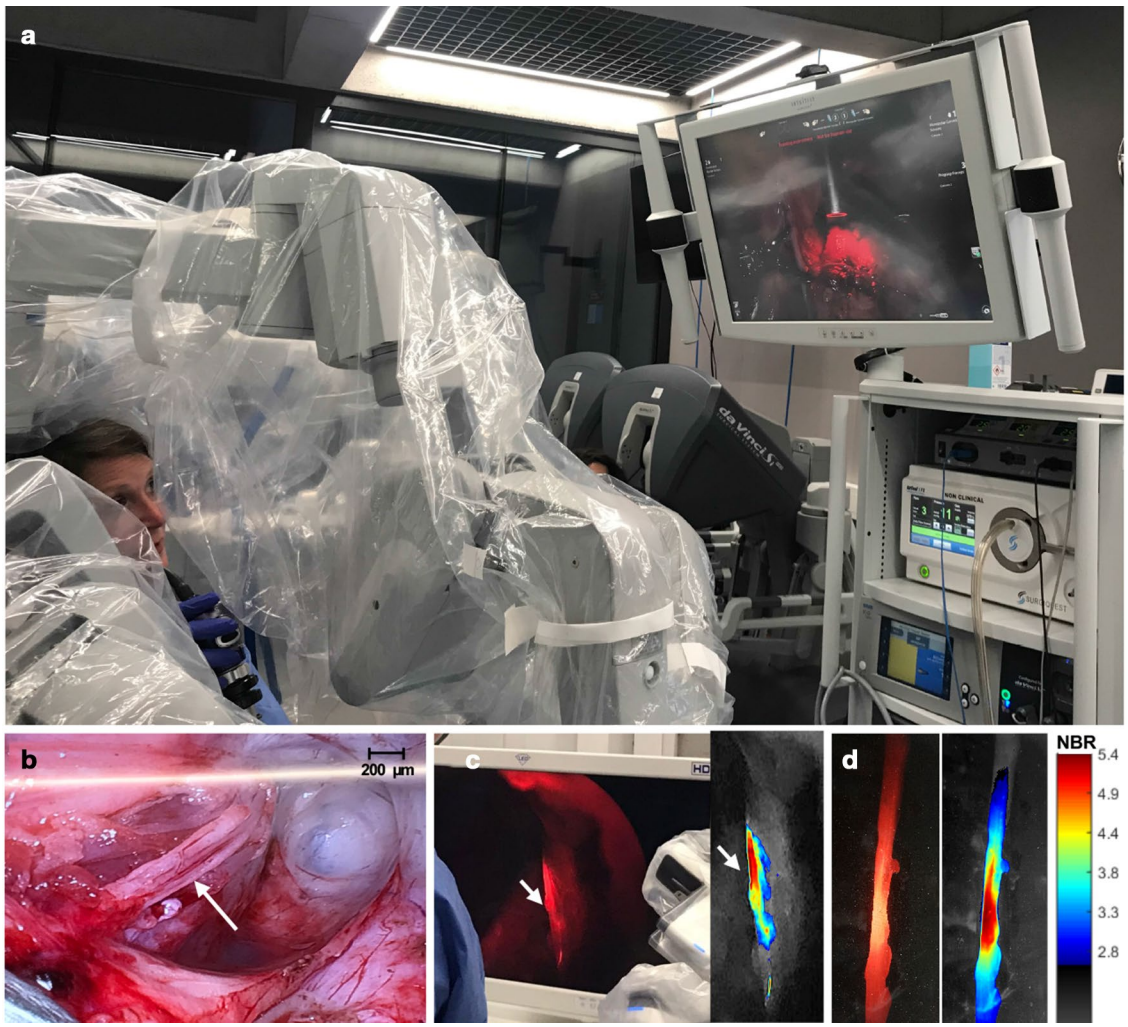

Fig. 6 Translation of Cy5-P0$_{101-125}$ into large animal models using clinical grade imaging modalities. **A** Surgical set-up showing the Da Vinci surgical robot and the use of a clinical grade STORZ fluorescence laparoscope dedicated for Cy5 imaging [42]. **B** Brightfield image of the pudendal nerve (white arrow). **C** In vivo fluorescence imaging of the pudendal nerve after intraneural administration of **Cy5-P0$_{101-125}$** as visible on the screen of the imaging set-up. Insert showing a colour-coded processed image of the fluorescence in the nerve. **D** Ex vivo fluorescence image of the excised nerve (left image) with corresponding colour-coded image-processing (right image) and scale bar depicting the corresponding nerve-to-background ratio (NBR)

vein (Fig. 4A), still provides further optimization before it can be used in a human setting. Hence, the exact route for local tracer administration in large animals, minimization of the dose and the specificity of targeting remain the subject of ongoing studies. Another potential limitation of the approach presented is that myelinization of nerves in the PNS may vary, where sensory nerves are highly myelinated (and conductive), the level of myelination decreases substantially in autonomous nerves. Despite the fact that myelin is one of the most widely explored targets for nerve imaging, it is therefore not clear if myelin-specific tracers will help address all surgical nerve imaging demands.

Conclusion

By truncating the P0 protein, we have been able to successfully create a nerve-specific fluorescent tracer that is able to specifically stain P0/myelin expression in the PNS.

Abbreviations

MPZ, or P0: Myelin protein zero; PNS: Peripheral nervous system; CNS: Central nervous system; PLP: Myelin proteolipid protein; 3D: Three-dimensional; DRG: Dorsal root ganglion; HPLC: High-pressure liquid chromatography; LRMS: Low-resolution mass spectrometry; SI: Supporting information; PBS: Phosphate-buffered saline; FLISA: Fluorescence-linked immunoabsorbent assay; NIR: Near-infrared.

Supplementary Information

The online version contains supplementary material available at https://doi.org/10.1186/s13550-021-00792-9.

Additional file 1. Errors regarding SI table/scheme references were corrected.

Authors' contributions

TB was performed in conceptualization, methodology, investigation, writing-original draft, writing-review and editing. AWH was involved in investigation, writing-original draft. DM W contributed to methodology, investigation, visualization, writing-original draft. FB done recourses, writing-review and editing. KB was involved in recourses and investigation. RCMP done writing-review and editing. FWBL contributed to conceptualization, methodology, writing-review and editing. All authors read and approved the final manuscript.

Funding

This work was financially supported by an ERC starting Grant (ILLUMINATING NERVES; 2012-306890) and an ERC proof-of-concept Grant (MY NERVE; 2017-693303) and a NWO-TTW-VICI (TTW BGT16141) Grant. Funding bodies did not influence the design of the study, data collection, analysis, and interpretation of data and in writing of the manuscript.

Availability of data and materials

The datasets used and/or analysed during the current study are available from the corresponding author on reasonable request.

Declarations

Ethical approval and consent to participate

All experiments in mice were approved by the local ethics committee of the LUMC (mouse model) and Gent University (porcine model) prior to execution. Experiments were performed in accordance with the Experiments on Animals Act (Wod, 2014), the applicable legislation in the Netherlands and Belgium in accordance with the European guidelines (EU directive no. 2010/63/EU) regarding the protection of animals used for scientific purposes. Mice and pigs were bred and kept in accordance with the Dutch and Belgium law in and by a licensed establishment for use of experimental animals. Experiments in pigs were approved by ethical board of the University of Ghent (EC2019/79). Pigs were housed at the animal facility at ORSI Academy (Melle, Belgium) until used for nerve imaging experiments during surgical training (weight per animal approximately 40 kg).

Consent for publication

Not applicable.

Competing interests

The authors declare that they have no competing interests.

Author details

[1]Interventional Molecular Imaging Laboratory, Department of Radiology, Leiden University Medical Center, Albinusdreef 2, 2300 RC Leiden, The Netherlands. [2]Neurologische Klinik, Heinrich-Heine University Dusseldorf, Düsseldorf, Germany. [3]ORSI Academy, Melle, Belgium. [4]Department of Urology, Leiden University Medical Center, Leiden, The Netherlands.

Received: 18 March 2021 Accepted: 17 May 2021
Published online: 29 May 2021

References

1. Maccormac W. The development of surgery. Science. 1900;12(294):254–63.
2. Autorino R, Porpiglia F, Dasgupta P, Rassweiler J, Catto JW, Hampton LJ, et al. Precision surgery and genitourinary cancers. Eur J Surg Oncol. 2017;43(5):893–908.
3. Checcucci E, Amparore D, De Luca S, Autorino R, Fiori C, Porpiglia F. Precision prostate cancer surgery: an overview of new technologies and techniques. Minerva Urol Nefrol. 2019;71(5):487–501.
4. Goh HK, Ng YH, Teo DT. Minimally invasive surgery for head and neck cancer. Lancet Oncol. 2010;11(3):281–6.
5. Hosseini A, Khoury AL, Esserman LJ. Precision surgery and avoiding overtreatment. Eur J Surg Oncol. 2017;43(5):938–43.
6. van Oosterom MN, Rietbergen DDD, Welling MM, van der Poel HG, Maurer T, van Leeuwen FWB. Recent advances in nuclear and hybrid detection modalities for image-guided surgery. Expert Rev Med Devices. 2019;16(8):711–34.
7. Cazzato RL, Garnon J, Shaygi B, Koch G, Tsoumakidou G, Caudrelier J, et al. PET/CT-guided interventions: indications, advantages, disadvantages and the state of the art. Minim Invasive Ther Allied Technol. 2018;27(1):27–32.
8. Peters TM. Image-guidance for surgical procedures. Phys Med Biol. 2006;51(14):R505–40.
9. Valdés Olmos RA, Rietbergen DD, Vidal-Sicart S, Manca G, Giammarile F, Mariani G. Contribution of SPECT/CT imaging to radioguided sentinel lymph node biopsy in breast cancer, melanoma, and other solid cancers: from "open and see" to "see and open." Q J Nucl Med Mol Imaging. 2014;58(2):127–39.
10. Chi C, Du Y, Ye J, Kou D, Qiu J, Wang J, et al. Intraoperative imaging-guided cancer surgery: from current fluorescence molecular imaging methods to future multi-modality imaging technology. Theranostics. 2014;4(11):1072–84.
11. van Leeuwen FWB, Schottelius M, Brouwer OR, Vidal-Sicart S, Achilefu S, Klode J, et al. Trending: radioactive and fluorescent bimodal/hybrid tracers as multiplexing solutions for surgical guidance. J Nucl Med. 2020;61(1):13–9.
12. KleinJan GH, van Werkhoven E, van den Berg NS, Karakullukcu MB, Zijlmans H, van der Hage JA, et al. The best of both worlds: a hybrid approach for optimal pre- and intraoperative identification of sentinel lymph nodes. Eur J Nucl Med Mol Imaging. 2018;45(11):1915–25.
13. Maurer T, Robu S, Schottelius M, Schwamborn K, Rauscher I, van den Berg NS, et al. (99m)Technetium-based prostate-specific membrane antigen-radioguided surgery in recurrent prostate cancer. Eur Urol. 2019;75(4):659–66.
14. Maurer T, Weirich G, Schottelius M, Weineisen M, Frisch B, Okur A, et al. Prostate-specific membrane antigen-radioguided surgery for metastatic lymph nodes in prostate cancer. Eur Urol. 2015;68(3):530–4.
15. Nishio N, van den Berg NS, van Keulen S, Martin BA, Fakurnejad S, Teraphongphom N, et al. Optical molecular imaging can differentiate metastatic from benign lymph nodes in head and neck cancer. Nat Commun. 2019;10(1):5044.
16. Voskuil FJ, de Jongh SJ, Hooghiemstra WTR, Linssen MD, Steinkamp PJ, de Visscher S, et al. Fluorescence-guided imaging for resection margin evaluation in head and neck cancer patients using cetuximab-800CW: a quantitative dose-escalation study. Theranostics. 2020;10(9):3994–4005.
17. Ficarra V, Sooriakumaran P, Novara G, Schatloff O, Briganti A, Van der Poel H, et al. Systematic review of methods for reporting combined outcomes after radical prostatectomy and proposal of a novel system: the survival, continence, and potency (SCP) classification. Eur Urol. 2012;61(3):541–8.
18. KleinJan GH, Sikorska K, Korne CM, Brouwer OR, Buckle T, Tillier C, et al. A prediction model relating the extent of intraoperative fascia preservation to erectile dysfunction after nerve-sparing robot-assisted radical prostatectomy. J Robot Surg. 2019;13(3):455–62.
19. Skarecky D, Morales B, Chang A, Ahlering T. Simple method to predict return of continence after robot-assisted radical prostatectomy. J Endourol. 2011;25(9):1451–5.
20. Buckle T, KleinJan GH, Engelen T, van den Berg NS, DeRuiter MC, van der Heide U, et al. Diffusion-weighted-preparation (D-prep) MRI as a future extension of SPECT/CT based surgical planning for sentinel node procedures in the head and neck area? Oral Oncol. 2016;60:48–54.
21. Godballe C, Madsen AR, Sørensen CH, Schytte S, Trolle W, Helweg-Larsen J, et al. Risk factors for recurrent nerve palsy after thyroid surgery: a national study of patients treated at Danish departments of ENT Head and Neck Surgery. Eur Arch Otorhinolaryngol. 2014;271(8):2267–76.
22. Møller MN, Sørensen CH. Risk of marginal mandibular nerve injury in neck dissection. Eur Arch Otorhinolaryngol. 2012;269(2):601–5.

23. Walsh EM, Cole D, Tipirneni KE, Bland KI, Udayakumar N, Kasten BB, et al. Fluorescence imaging of nerves during surgery. Ann Surg. 2019;270(1):69–76.
24. Barth CW, Gibbs SL. Direct administration of nerve-specific contrast to improve nerve sparing radical prostatectomy. Theranostics. 2017;7(3):573–93.
25. Gibbs-Strauss SL, Nasr KA, Fish KM, Khullar O, Ashitate Y, Siclovan TM, et al. Nerve-highlighting fluorescent contrast agents for image-guided surgery. Mol Imaging. 2011;10(2):91–101.
26. Park MH, Hyun H, Ashitate Y, Wada H, Park G, Lee JH, et al. Prototype nerve-specific near-infrared fluorophores. Theranostics. 2014;4(8):823–33.
27. Whitney MA, Crisp JL, Nguyen LT, Friedman B, Gross LA, Steinbach P, et al. Fluorescent peptides highlight peripheral nerves during surgery in mice. Nat Biotechnol. 2011;29(4):352–6.
28. Hingorani DV, Whitney MA, Friedman B, Kwon JK, Crisp JL, Xiong Q, et al. Nerve-targeted probes for fluorescence-guided intraoperative imaging. Theranostics. 2018;8(15):4226–37.
29. Hussain T, Mastrodimos MB, Raju SC, Glasgow HL, Whitney M, Friedman B, et al. Fluorescently labeled peptide increases identification of degenerated facial nerve branches during surgery and improves functional outcome. PLoS ONE. 2015;10(3):e0119600.
30. Gustafson TP, Yan Y, Newton P, Hunter DA, Achilefu S, Akers WJ, et al. A NIR dye for development of peripheral nerve targeted probes. Medchemcomm. 2012;3(6):685–90.
31. D'Urso D, Brophy PJ, Staugaitis SM, Gillespie CS, Frey AB, Stempak JG, et al. Protein zero of peripheral nerve myelin: biosynthesis, membrane insertion, and evidence for homotypic interaction. Neuron. 1990;4(3):449–60.
32. Boison D, Büssow H, D'Urso D, Müller HW, Stoffel W. Adhesive properties of proteolipid protein are responsible for the compaction of CNS myelin sheaths. J Neurosci. 1995;15(8):5502–13.
33. Makowska A, Pritchard J, Sanvito L, Gregson N, Peakman M, Hayday A, et al. Immune responses to myelin proteins in Guillain–Barré syndrome. J Neurol Neurosurg Psychiatry. 2008;79(6):664–71.
34. Haack T, Mutter M. Serine derived oxazolidines as secondary structure disrupting, solubilizing building blocks in peptide synthesis. Tetrahedron Lett. 1992;33(12):1589–92.
35. Hai M, Muja N, DeVries GH, Quarles RH, Patel PI. Comparative analysis of Schwann cell lines as model systems for myelin gene transcription studies. J Neurosci Res. 2002;69(4):497–508.
36. Buckle T, van Willigen DM, Spa SJ, Hensbergen AW, van der Wal S, de Korne CM, et al. Tracers for fluorescence-guided surgery: how elongation of the polymethine chain in cyanine dyes alters the pharmacokinetics of a dual-modality c[RGDyK] tracer. J Nucl Med. 2018;59(6):986–92.
37. Buckle T, van der Wal S, van Willigen DM, Aalderink G, KleinJan GH, van Leeuwen FWB. Fluorescence background quenching as a means to increase Signal to Background ratio—a proof of concept during Nerve Imaging. Theranostics. 2020;10(21):9890–8.
38. van der Wal S, de Korne CM, Sand LGL, van Willigen DM, Hogendoorn PCW, Szuhai K, et al. Bioorthogonally applicable fluorescence deactivation strategy for receptor kinetics study and theranostic pretargeting approaches. ChemBioChem. 2018;19(16):1758–65.
39. de Vries HMB E, van Oosterom MN, Karakullukcu MB, van der Poel HG, van Leeuwen FWB, Buckle T, Brouwer OR. c-MET receptor-targeted fluorescence-guided surgery—first experience in penile squamous cell carcinoma patients, a phase IIa study. JNM 2021. Accepted for publication.
40. Bunschoten A, van Willigen DM, Buckle T, van den Berg NS, Welling MM, Spa SJ, et al. Tailoring fluorescent dyes to optimize a hybrid RGD-Tracer. Bioconjug Chem. 2016;27(5):1253–8.
41. Hensbergen AW, Buckle T, van Willigen DM, Schottelius M, Welling MM, van der Wijk FA, et al. Hybrid tracers based on cyanine backbones targeting prostate-specific membrane antigen: tuning pharmacokinetic properties and exploring dye-protein interaction. J Nucl Med. 2020;61(2):234–41.
42. van Willigen DM, van den Berg NS, Buckle T, KleinJan GH, Hardwick JC, van der Poel HG, et al. Multispectral fluorescence guided surgery; a feasibility study in a phantom using a clinical-grade laparoscopic camera system. Am J Nucl Med Mol Imaging. 2017;7(3):138–47.
43. KleinJan GH, van den Berg NS, Brouwer OR, de Jong J, Acar C, Wit EM, et al. Optimisation of fluorescence guidance during robot-assisted laparoscopic sentinel node biopsy for prostate cancer. Eur Urol. 2014;66(6):991–8.
44. van der Poel HG, Buckle T, Brouwer OR, Valdes Olmos RA, van Leeuwen FW. Intraoperative laparoscopic fluorescence guidance to the sentinel lymph node in prostate cancer patients: clinical proof of concept of an integrated functional imaging approach using a multimodal tracer. Eur Urol. 2011;60(4):826–33.
45. Sung SS. Peptide folding driven by Van der Waals interactions. Protein Sci. 2015;24(9):1383–8.
46. Melli G, Höke A. Dorsal root ganglia sensory neuronal cultures: a tool for drug discovery for peripheral neuropathies. Expert Opin Drug Discov. 2009;4(10):1035–45.
47. Hensbergen AW, van Willigen DM, van Beurden F, van Leeuwen PJ, Buckle T, Schottelius M, et al. Image-guided surgery: are we getting the most out of small-molecule prostate-specific-membrane-antigen-targeted tracers? Bioconjug Chem. 2020;31(2):375–95.
48. Kuil J, Buckle T, van Leeuwen FW. Imaging agents for the chemokine receptor 4 (CXCR4). Chem Soc Rev. 2012;41(15):5239–61.
49. Chen K, Chen X. Design and development of molecular imaging probes. Curr Top Med Chem. 2010;10(12):1227–36.
50. Staderini M, Megia-Fernandez A, Dhaliwal K, Bradley M. Peptides for optical medical imaging and steps towards therapy. Bioorg Med Chem. 2018;26(10):2816–26.
51. KleinJan GH, Bunschoten A, van den Berg NS, Olmos RA, Klop WM, Horenblas S, et al. Fluorescence guided surgery and tracer-dose, fact or fiction? Eur J Nucl Med Mol Imaging. 2016;43(10):1857–67.
52. Rosenthal EL, Warram JM, de Boer E, Basilion JP, Biel MA, Bogyo M, et al. Successful translation of fluorescence navigation during oncologic surgery: a consensus report. J Nucl Med. 2016;57(1):144–50.
53. Nishio N, van den Berg NS, van Keulen S, Martin BA, Fakurnejad S, Zhou Q, et al. Optimal dosing strategy for fluorescence-guided surgery with Panitumumab-IRDye800CW in head and neck cancer. Mol Imaging Biol. 2020;22(1):156–64.
54. Tummers QR, Hoogstins CE, Gaarenstroom KN, de Kroon CD, van Poelgeest MI, Vuyk J, et al. Intraoperative imaging of folate receptor alpha positive ovarian and breast cancer using the tumor specific agent EC17. Oncotarget. 2016;7(22):32144–55.
55. van Leeuwen FW, Valdes-Olmos R, Buckle T, Vidal-Sicart S. Hybrid surgical guidance based on the integration of radionuclear and optical technologies. Br J Radiol. 2016;89(1062):20150797.
56. van Leeuwen FW, Hardwick JC, van Erkel AR. Luminescence-based imaging approaches in the field of interventional molecular imaging. Radiology. 2015;276(1):12–29.
57. Burggraaf J, Kamerling IM, Gordon PB, Schrier L, de Kam ML, Kales AJ, et al. Detection of colorectal polyps in humans using an intravenously administered fluorescent peptide targeted against c-Met. Nat Med. 2015;21(8):955–61.
58. de Jongh SJ, Vrouwe JPM, Voskuil FJ, Schmidt I, Westerhof J, Koornstra JJ, et al. The optimal imaging window for dysplastic colorectal polyp detection using c-Met-targeted fluorescence molecular endoscopy. J Nucl Med. 2020;61(10):1435–41.
59. Zanoni DK, Stambuk HE, Madajewski B, Montero PH, Matsuura D, Busam KJ, et al. Use of ultrasmall core-shell fluorescent silica nanoparticles for image-guided sentinel lymph node biopsy in head and neck melanoma: a nonrandomized clinical trial. JAMA Netw Open. 2021;4(3):e211936.
60. van Beurden F, van Willigen DM, Vojnovic B, van Oosterom MN, Brouwer OR, der Poel HGV, et al. Multi-wavelength fluorescence in image-guided surgery, clinical feasibility and future perspectives. Mol Imaging. 2020;19:1536012120962333.
61. Haw SSJ, van der Wal S, Kuil J, van Leeuwen FWB. The influence of systematic structure alterations on the photo-physical properties and conjugation characteristics of asymmetric cyanine 5 dyes. Dyes Pigm. 2018;152:19–28.

Publisher's Note